International Society for Rock Mechanics and Rock Engineering
Norwegian Group for Rock Mechanics

ISRM International Symposium
Eurock 2025 – Expanding the Underground Space
Trondheim, Norway, 16-20 June
ISBN 978-82-8208-079-8

Experimental Assessment of the Geomechanical Properties of Mowry Shale

E. Dabbaghi, K. Ng, J. Romero, & V. Alvarado
University of Wyoming, Laramie, USA
kng1@uwyo.edu

Abstract

Shale reservoirs have attracted attention as an energy source due to the growing energy demand. The oil and gas industry has significantly benefited from the use of horizontal drilling and hydraulic fracturing in shale reservoirs. Mowry shale is regarded as a major source of Cretaceous oil and gas in the northern Rocky Mountains. While it is considered an important hydrocarbon source rock, the geomechanical behaviour of Mowry shale has yet to be thoroughly investigated. This paper aims to shed light on the mechanical properties of Mowry shale. For this study, Mowry shale samples from well S505 in Wyoming (core stored at the United States Geological Survey (USGS)), at a depth of about 3250 m were acquired. Each sample was encased in a concrete box prior to dried drilling. A total of three specimens with a diameter of 12.5 mm and a height of 25 mm were drilled out of the original samples. The specimens were treated with a Formation aqueous phase for 35 days. Triaxial compression tests were conducted on the specimens using GCTS-RTR 1500 equipment. Three confining pressures of 12, 26, and 40 MPa, and a pore pressure of 9 MPa at 96 °C were adopted in the triaxial testing. This paper presents the stress-strain behaviour of brine-saturated Mowry shale specimens subjected to different effective confining pressures. Results will improve the understanding of Mowry shale mechanical behaviour and properties, which are pivotal for oil production in unconventional reservoirs.

Keywords

Unconventional reservoir, Shale formations, Rock mechanics, Fracturing fluid, Mechanical properties

1 Introduction

Interest in shale reservoirs as an energy source has grown in response to increasing energy demands (Wang et al. 2016). A thorough understanding of shale reservoir geomechanics can enhance production efficiency. Numerous studies have been dedicated to exploring the mechanical properties of shale. Researchers have examined the impact of confining pressure on shale samples' mechanical behaviour. For instance, as confining pressure increased from 20 to 30 MPa, Pierre-1 shale samples exhibited a 53% increase in peak strength (Islam and Skalle 2013). Similarly, a rise in confining pressure from 20 to 80 MPa enhanced the peak strength of marine shale samples from 160 to 300 MPa, marking an 88% increase (Wang et al. 2022). Additionally, studies have explored surface morphology alterations post-treatment with fracturing fluids. Tan et al. (2022) reported that fractal dimensions of Niutitang black shale increased by 9-30% following fracturing fluid imbibition due to dissolution, hydrolysis, and hydration processes. Sun et al. (2018) observed rougher surfaces on Longmaxi shale samples after a 72-hour reaction with slick water, attributed to carbonate dissolution.

Mowry shale is recognized as a key source of Cretaceous oil and gas across the northern Rocky Mountain Region in the United States, with hydrocarbons particularly concentrated in Lower Cretaceous reservoirs. Mowry shale Formations are located in the Wind River Basin Province, Bighorn Basin, and Powder River Basin in Wyoming, USA (Dabbaghi et al. 2024). Despite its significance as a source rock for oil and gas, the geomechanical properties of Mowry shale remain largely unexplored, posing challenges for unconventional hydrocarbon extraction (Pish 2014). This study examines the stress-strain behaviour of Mowry shale under varying effective confining pressures through triaxial compression (TC) tests, offering insights that enhance our understanding of its geomechanical characteristics.

2 Geological Formation

The Mowry shale Formation, a biogenic siliceous mudstone from the Lower Cretaceous period, spans much of western North America and includes major basins in Wyoming. This Formation was deposited during a time when the Mowry Sea covered a large portion of western North America, stretching from the Arctic down to present-day Colorado (Byers and Larson 1979; Davis 1970; Davis, Byers, and Pratt 1989). The depositional environment of the Mowry shale was helpful to the production of silica-bearing radiolarians, while limited access to warmer southern waters inhibited carbonate deposition (Davis 1970; Davis et al. 1989). This depositional setting produced a shale with notably high silica and low carbonate content. The silica in Mowry shale is mainly of biogenic origin, with evidence suggesting a combination of both detrital and biogenic sources (French, Birdwell, and Lillis 2023; Hollon 2014; Milliken and Olson 2017). The Mowry shale serves as a significant hydrocarbon source rock in Wyoming's Powder River Basin, making it a target of interest for direct hydrocarbon production (Davis et al. 1989; French et al. 2023; Nixon 1973). The Mowry shale is lithologically classified as a biogenic siliceous mudstone. While facies divisions vary based on the author, common considerations include bentonite presence, sand content, degree of lamination, and silica origin, whether biogenic or detrital (Davis 1970; Davis et al. 1989; Hollon 2014; Socianu 2016).

3 Experimental Methods

3.1 Sample Collection and Specimen Preparation

Samples of Mowry shale were obtained from the United States Geological Survey (USGS) collection in Denver, USA, specifically from library number S505, at depths between 3230 and 3243 m. These heavily layered and brittle samples could not support conventional core drilling for larger specimens. Instead, smaller-diameter cores were extracted from the original samples. Each Mowry shale piece wrapped with a plastic membrane was placed within a cube mould, and mortar was poured around it to create a stable confinement to drilling. After one week, the mortar was hardened for drilling, and 12.5-mm diameter plugs were successfully obtained. Three specimens with lengths twice their diameter were prepared, and cut to size using a wet saw. Both ends were then smoothened using a surface grinder to ensure even, perpendicular surfaces.

Fig. 1. Photos show the specimen preparation steps.

3.2 Rock Treatment

The specimens were aged in Formation water under conditions designed to simulate the Formation's in-situ environment, with a pressure of 9 MPa and a temperature of 96 °C. Prior to aging, all specimens were vacuum-saturated with Formation brine over four days to ensure full saturation in these low-permeability rocks. After saturation, the shale samples were placed in a transfer vessel filled with Formation brine. The vessel had two chambers separated by a tightly sealed plug: the lower chamber (inlet) connected to an ISCO pump for pressure control via DI water volume adjustments, and the upper chamber (outlet) which held the Formation brine and shale samples. Once sealed, the vessel was transferred to an oven set to the target in-situ temperature, and the Formation brine-rock interaction experiment was maintained for 35 days. Following this period, the shale samples were removed from the vessel and desaturated to prepare them for geomechanical testing.

3.3 Triaxial Compression Tests

Table 1 outlines the experimental conditions for the geomechanical tests conducted on the specimens. The identification system for the specimens was based on triaxial compression parameters, including confining and pore pressures, with an in-situ temperature set at 96 °C. Triaxial compression tests were performed using the newly retrofitted GCTS RTR-1500 equipment, adapted to accommodate 12.5-mm diameter specimens (see Fig. 2a). Each specimen was secured between two holders and encased in a heat shrink jacket to prevent contamination between the confining oil and the pore pressure water during testing. Axial deformations were monitored using two linear variable differential transformers (LVDTs) mounted on a ring, while three additional LVDTs on a middle ring recorded radial deformations (Fig. 2b). The specimen column was then inserted into the equipment, and the cell wall was lowered. The cell was filled with oil, which was heated to the target temperature within approximately two hours. Initially, a confining pressure of about 2 MPa was applied, along with a small deviatoric stress of around 1 MPa. A pore pressure of 0.17 MPa was also introduced. Subsequently, both confining and pore pressures were ramped up to their target values over a period of 5 minutes, while the deviatoric stress was constant. After holding the confining and pore pressures in equilibrium for 5 minutes, the deviatoric stress was increased at a rate of 0.1% axial strain per minute until failure occurred. Failure was indicated by a decrease in axial stress with a continued increase in axial strain.

Table 1. Summary of the experiment conditions for the specimens.

Specimen ID	Diameter (mm)	Length (mm)	Dry Weight (g)	Wet Weight (g)	Depth (m)	Confining Pressure (MPa)	Pore Pressure (MPa)	Effective Pressure (MPa)
TC1	11.68	26.92	6.89	7.01	3234	12.4	9	3.4
TC2		27.18	7.18	7.23	3234	26.2		17.2
TC3		28.7	7.52	7.58	3235	40		31.0

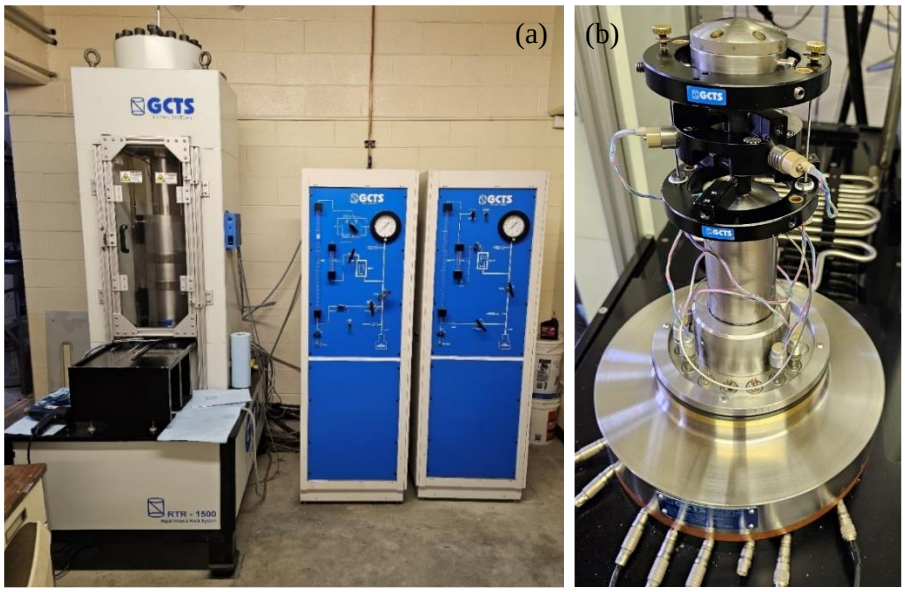

Fig. 2. a) The GCTS RTR-1500 equipment at the University of Wyoming, and b) the 12.5-mm diameter specimen set up with two axial and three radial LVDTs.

4 Results and Discussion

4.1 Confining Stage

4.1.1 Changes in Volumetric Strain

Figure 3 illustrates the relationship between volumetric strain (ε_v) and effective confining pressure (P_d) for the specimens during the confinement phase of the triaxial compression tests. The volumetric strain was calculated using Eq. (1), based on the measured radial strain (ε_r) and axial strain (ε_a), while the effective confining pressure was determined using Eq. (2) as the difference between confining pressure (P_c) and pore pressure (P_p). The results indicate that ε_v increases with rising P_d for all specimens. Specimen TC1 reached a maximum ε_v of 0.33%. When the P_d for specimen TC2 was increased to 17 MPa, it exhibited a maximum ε_v of 0.6%. Specimen TC3 recorded the highest maximum ε_v at 0.87% at the highest P_d of 31 MPa. The observed positive trend in ε_v indicates compression within the specimens during the confinement stage.

$$\varepsilon_v = 2\varepsilon_r + \varepsilon_a \tag{1}$$

$$P_d = P_c - P_p \tag{2}$$

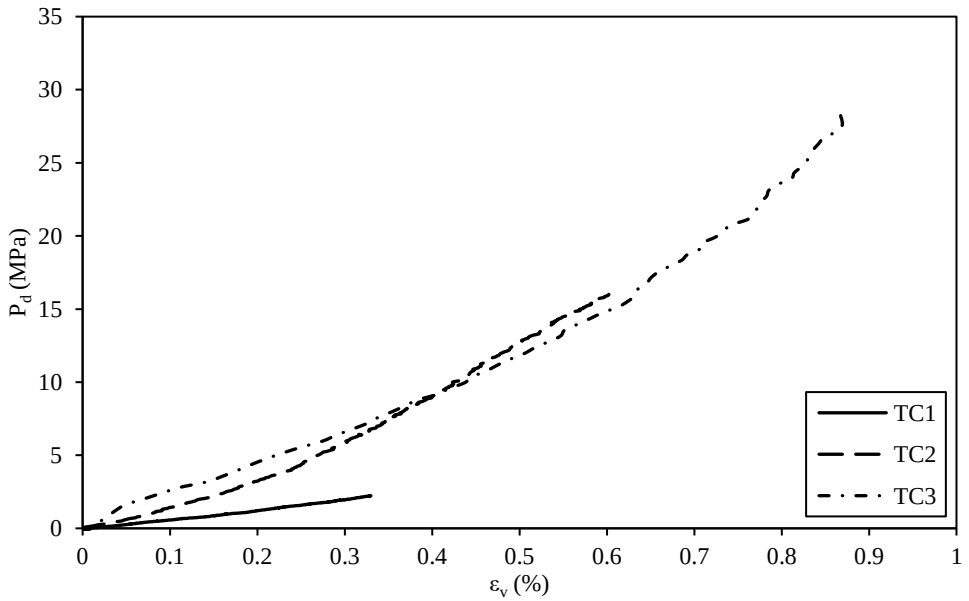

Fig. 3. The relationships of the volumetric strain (ε_v) and the effective confining pressure (P_d).

4.1.2 Bulk Modulus

The Bulk Modulus (K), which serves as an indicator of the change in the specimen's volume during the confinement stage, was calculated using Eq. (3). This calculation is based on the change in effective confining pressure (ΔP_d) with respect to the change in volumetric strain ($\Delta \varepsilon_v$).

$$K = \frac{\Delta P_d}{\Delta \varepsilon_v} \tag{3}$$

Figure 4 presents the relationship between bulk modulus (K) and effective confining pressure (P_d) for all specimens. It is evident that specimens subjected to higher P_d exhibit elevated K. The K value for specimen TC1 is 0.68 GPa, while the K value of specimen TC2 rises to 2.66 GPa. Specimen TC3 demonstrates the highest K value at 3.29 GPa. The trend of higher K values corresponding to increased P_d aligns with the lower maximum ε_v observed in those specimens, as illustrated in Figure 3.

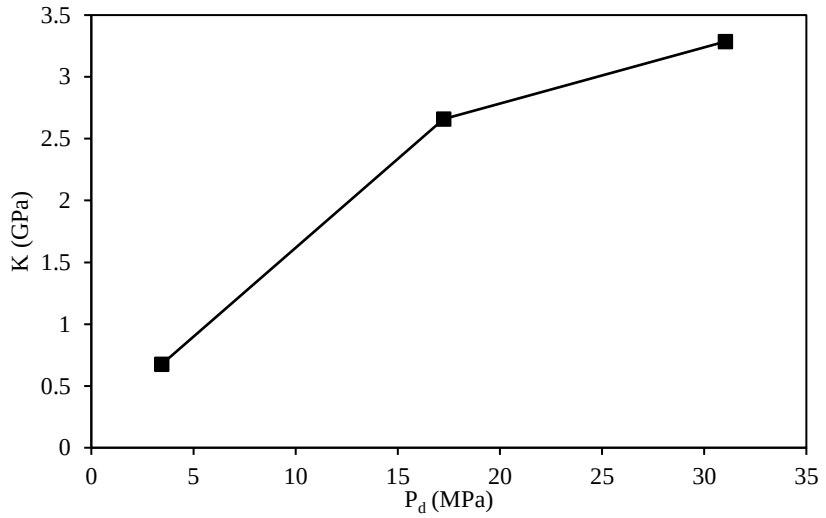

Fig. 4. Relationship between bulk modulus (K) and the effective confining pressure (P_d).

4.2 Axial Loading Stage

4.2.1 Axial Stress-Strain Responses

Figure 5 displays the relationship between deviatoric axial stress ($\Delta\sigma_d$) and both axial strain (ε_a) and radial strain (ε_r) for the specimens. Each plot illustrates the $\Delta\sigma_d$-ε_r response on the left and the $\Delta\sigma_d$-ε_a response on the right. Positive ε_a signifies axial compression, while negative ε_r indicates the radial expansion of the shale specimen under axial loading. As the plot shows, the maximum $\Delta\sigma_d$ observed in the specimens increases with higher P_d. Specimen TC1 reaches a peak strength of 70 MPa, whereas specimen TC2, with increased P_d, achieves a peak strength of approximately 218 MPa. The highest peak strength is recorded for specimen TC3 at 231 MPa. The increase in P_d causes the specimens to fail at higher ε_a values. All specimens exhibit a brittle failure mode while TC3 begins to exhibit a post failure ductile behaviour due to a higher P_d of 31 MPa.

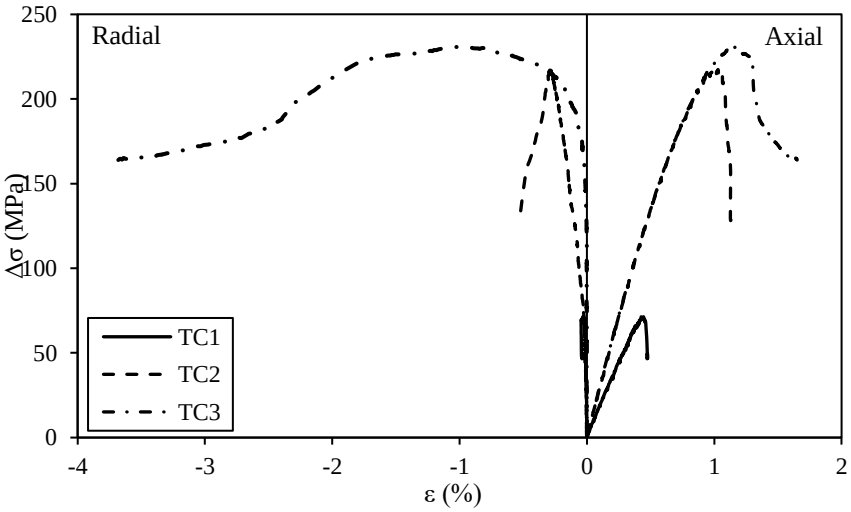

Fig. 5. Stress-strain responses of the specimens.

4.2.2 Elastic Constants

Figure 6 shows the elastic modulus (E) and Poisson's ratio (ν) in relation to effective confining pressure (P_d). For each specimen, a straight line was fitted to the linear segment of the stress-strain curve (Figure 5), with the slope of this line representing the elastic modulus (E). Poisson's ratio (ν) was calculated using Eq. (4), based on the measured radial strain (ε_r) and axial strain (ε_a) from the linear region of the stress-strain responses depicted in Figure 5.

$$\nu = -\frac{\varepsilon_r}{\varepsilon_a} \tag{4}$$

Figure 6 shows that as P_d increases, the elastic modulus (E) of the specimens also rises. At the lowest P_d, a recorded E value of 17 GPa is observed. Specimens TC2 and TC3 exhibit E values of 24 GPa. Regarding Poisson's ratio, specimen TC1 has a value of 0.03. Specimen TC2 shows a higher Poisson's ratio of 0.21, likely due to the softening effect associated with increased confining pressure. At the highest P_d, specimen TC3 has a Poisson's ratio of 0.08, which could be attributed to higher P_d constraining the radial strain.

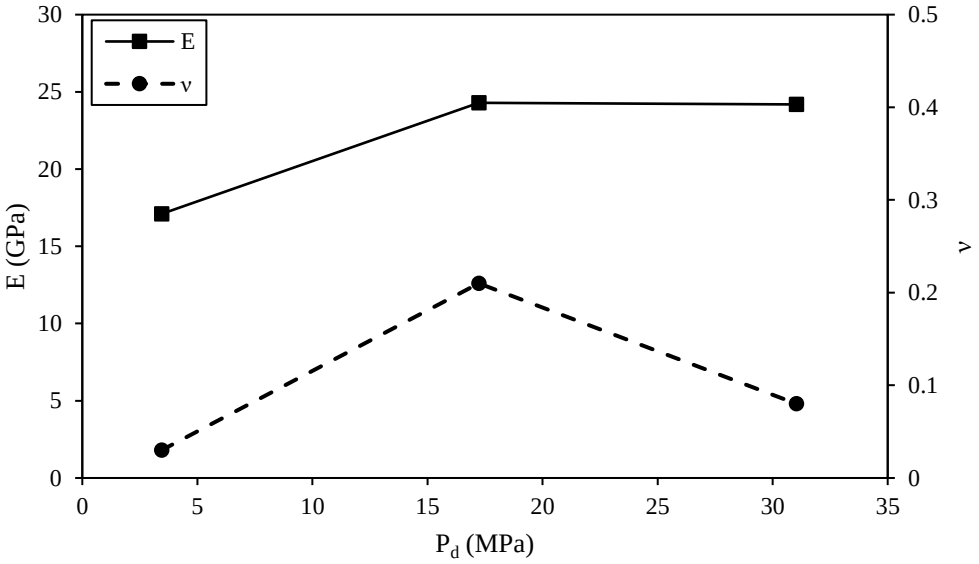

Fig. 6. Comparison of elastic modulus (E) and Poisson's ratio (ν).

4.2.3 Major and Minor Effective Principal Stresses

Figure 7 illustrates the relationship between the major effective principal stress (P'_a) and the minor effective principal stress (P_d) for the specimens. The major effective principal stress (P'_a) is calculated using Eq. (5), which represents the sum of the minor effective principal stress (P_d) and the maximum deviatoric stress ($\Delta\sigma_d$).

$$P'_a = P_d + \Delta\sigma_d \tag{5}$$

Figure 7 demonstrates that an increase in P_d leads to a rise in P'_a for the specimens. At a P_d of 3.4 MPa, the specimen exhibits a P'_a of 75 MPa. When P_d increases to 17 MPa, the P'_a value rises to 235 MPa. At the maximum P_d of 31 MPa, a P'_a value of 262 MPa is recorded.

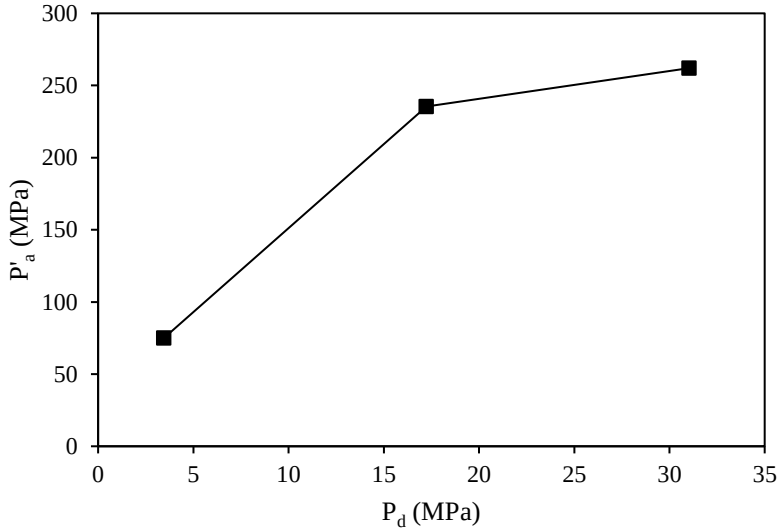

Fig. 7. The relationships between major (P'_a) and minor (P_d) effective principal stresses.

4.2.4 Shear Strength Parameters

The effective friction angle (φ') can be determined using Eq. (6), which is based on the slope (a) of the linear fitted line representing the relationship between major effective principal stress (P'_a) and minor effective principal stress (P_d) as shown in Figure 7. The effective cohesion (c') is then calculated using Eq. (7), which utilizes the y-intercept value (b) of the fitted line along with the previously calculated φ'. The calculations yielded an effective friction angle (φ') of 48° and an effective cohesion (c') of 14 MPa for the specimens.

$$\varphi' = \sin^{-1}\left(\frac{a-1}{a+1}\right) \tag{6}$$

$$c' = \frac{b(1-\sin\varphi')}{2\cos\varphi'} \tag{7}$$

5 Conclusions

The following conclusions are drawn from this study:

1. All Mowry shale specimens show a rise in volumetric strain (ε_v) as the effective confining pressure (P_d) increases.
2. Specimens subjected to higher P_d demonstrate greater bulk moduli (K).
3. The maximum deviatoric axial stress ($\Delta\sigma_d$) of the specimens increases with higher P_d.
4. All specimens failed in a brittle manner with the specimen TC3 subjected to the highest P_d of 31 MPa began to exhibit a post failure ductile behaviour.
5. Specimens tested at elevated P_d exhibit higher elastic modulus (E) and major effective principal stress (P'_a) values.
6. The Poisson's ratio (ν) of the specimens is influenced by the effective confining pressure (P_d).

References

Byers, Charles W., and David W. Larson. 1979. 'GEOLOGIC NOTES Paleoenvironments of Mowry Shale (Lower Cretaceous), Western and Central Wyoming'. *AAPG Bulletin* 63(3):354–61.

Dabbaghi, Ehsan, Kam Ng, Zuhao Kou, Grant Copeland, and Vladimir Alvarado. 2024. 'Experimental Investigation to Understand the Effect of Fracturing Fluid on the Geomechanical Behavior of Mowry Shale'. *Journal of Petroleum Exploration and Production Technology*. doi: 10.1007/s13202-024-01788-6.

Davis, Hugh R., Charles W. Byers, and Lisa M. Pratt. 1989. 'Depositional Mechanisms and Organic Matter in Mowry Shale (Cretaceous), Wyoming'. *AAPG Bulletin* 73(9):1103–16.

Davis, John Clements. 1970. 'Petrology of Cretaceous Mowry Shale of Wyoming'. *AAPG Bulletin* 54(3):487–502.

French, Katherine L., Justin E. Birdwell, and Paul G. Lillis. 2023. 'Geochemistry of the Cretaceous Mowry Shale in the Wind River Basin, Wyoming'. *Bulletin* 135(7–8):1899–1922.

Hollon, Zachary Grant. 2014. *Elemental Chemostratigraphy and Reservoir Properties of the Mowry Shale in the Bighorn and Powder River Basins, Wyoming, USA*. Colorado School of Mines.

Islam, Md Aminul, and Paal Skalle. 2013. 'An Experimental Investigation of Shale Mechanical Properties through Drained and Undrained Test Mechanisms'. *Rock Mechanics and Rock Engineering* 46(6):1391–1413. doi: 10.1007/s00603-013-0377-8.

Milliken, Kitty L., and Terrilyn Olson. 2017. 'Silica Diagenesis, Porosity Evolution, and Mechanical Behavior in Siliceous Mudstones, Mowry Shale (Cretaceous), Rocky Mountains, USA'. *Journal of Sedimentary Research* 87(4):366–87.

Nixon, R. P. 1973. 'Oil Source Beds in Cretaceous Mowry Shale of Northwestern Interior United States'. *AAPG Bulletin* 57(1):136–61.

Pish, T. 2014. 'Regional Spotlight: Powder River Basin'. *Oil & Gas Investor, v. 32*, 1.

Socianu, Alexa L. 2016. 'Geochemical Insights into the Distribution of Organic Matter in the Mowry Shale'. *Southern Powder River Basin, Wyoming [MS Thesis]: Laramie, Wyoming, University of Wyoming*.

Sun, Zepeng, Hailong Zhang, Zhifu Wei, Yongli Wang, Baoxiang Wu, Shengguang Zhuo, Zhe Zhao, Jing Li, Lewei Hao, and Hui Yang. 2018. 'Effects of Slick Water Fracturing Fluid on Pore Structure and Adsorption Characteristics of Shale Reservoir Rocks'. *Journal of Natural Gas Science and Engineering* 51:27–36. doi: 10.1016/j.jngse.2017.12.030.

Tan, Jingqiang, Chenger Hu, Qiao Lyu, Gan Feng, and Shefa Chen. 2022. 'Experimental Investigation on the Effects of Different Fracturing Fluids on Shale Surface Morphology'. *Journal of Petroleum Science and Engineering* 212. doi: 10.1016/j.petrol.2022.110356.

Wang, Hongjun, Feng Ma, Xiaoguang Tong, Zuodong Liu, Xinshun Zhang, Zhenzhen Wu, Denghua Li, Bo Wang, Yinfu Xie, and Liuyan Yang. 2016. 'Assessment of Global Unconventional Oil and Gas Resources'. *Petroleum Exploration and Development* 43(6):925–40. doi: 10.1016/S1876-3804(16)30111-2.

Wang, Lei, Yintong Guo, Xiaogui Zhou, Guangguo Yang, Chunhe Yang, and Jialin Xiao. 2022. 'Mechanical Properties of Marine Shale and Its Roof and Floor Considering Reservoir Preservation and Stimulation'. *Journal of Petroleum Science and Engineering* 211. doi: 10.1016/j.petrol.2022.110194.